Institut für Numerische Simulation

Rheinische Friedrich-Wilhelms-Universität Bonn

M. Burkow, M. Griebel

A full three dimensional numerical simulation of the sediment transport and the scouring at a rectangular obstacle

A full three dimensional numerical simulation of the sediment transport and the scouring at a rectangular obstacle

M. Burkow[a], M. Griebel[a]

[a]*Institute for Numerical Simulation, University of Bonn, Wegelerstrasse 6, 53115 Bonn, Germany*

Abstract

We employ a numerical simulation of the three-dimensional fluid flow and the simultaneous transport of sediment to reproduce current-driven sediment transport processes. In particular, the scouring at a rectangular obstacle is investigated. To solve the instationary incompressible Navier-Stokes equations we use the code NaSt3D. The morphological change of the sediment bed is modelled by Exner's bed level equation, which is discretized and coupled to the discrete fluid model, i.e., to the NaSt3D code. A large eddy turbulence approach using a Smagorinsky subgrid scale tensor is applied. For our purposes, we only consider bed load transport under clear water conditions. Furthermore, we demonstrate mass conservation and convergence of our approach for a test case. We compare the results of our numerical simulations for a scour mark with those obtained in a laboratory flume. The typical sedimentary processes and the sedimentary form of a scour mark are well captured by our numerical simulation.

Email addresses: `burkow@ins.uni-bonn.de` (M. Burkow), `griebel@ins.uni-bonn.de` (M. Griebel)

1. Introduction

Sediment transport processes and scouring effects are significant issues in hydraulic engineering. Usually, the physical processes of forming scour marks and sedimentary forms are studied in laboratory flumes. Such experiments are however time-intensive, costly and not always easy to conduct. Here, numerical simulation can help to reduce costs and to obtain a better understanding of the relevant flow and transport phenomena.

Fluvial obstacle marks are mainly generated by bed load transport, which is a driving constituent of sediment transport (Zanke, 2002). In case of a scour mark, sediment is entrained in front of an obstacle, the luff, and transported in the bed load layer around the obstacle. If the velocity then gets smaller than a critical value, sediment is deposited in the lee. The type of transport under clear water conditions is almost exclusively reptation. The involved processes and the resulting depositional bedforms are strictly three-dimensional. We present a numerical approach for their simulation and discuss the obtained results.

The remainder of this paper is organized as follows. In section two, we describe the fluid-sediment-model, which consists of the Navier-Stokes equations, the turbulence modelling approach, and Exner's bed level equation. In section three, we shortly discuss the numerical discretization and its properties. In section four, we compare the results of our numerical simulations to a scour mark studied in a laboratory flume. Some conlcuding remarks are

2

given in section five.

2. Model: Navier–Stokes & Exner's bed level equation

Due to the complex three-dimensional character of the scour mark and other bedforms, it is necessary to use a full three-dimensional flow model. To this end, we use a single phase model. Here, for the flow problem, the instationary incompressible Navier-Stokes equations in their dimensionless form read as

$$\frac{\partial \mathbf{u}}{\partial t} + \nabla \cdot (\mathbf{u} \otimes \mathbf{u}) = \frac{1}{Fr}\mathbf{g} - \nabla p + \frac{1}{Re}\Delta \mathbf{u} \qquad in \quad \Omega_f \in \mathbb{R}^3, \qquad (1a)$$

$$\nabla \cdot \mathbf{u} = 0 \qquad in \quad \Omega_f \in \mathbb{R}^3, \qquad (1b)$$

where $\mathbf{u}$ denotes the velocity, p the pressure, $\mathbf{g}$ the volume forces.

$$Re = \frac{\mathbf{u}_\infty \cdot d}{\nu} \qquad (2)$$

denotes Reynolds number and

$$Fr = \frac{\mathbf{u}_\infty}{\sqrt{g \cdot d}} \qquad (3)$$

the Froude number. Both numbers, Re as well as Fr, are dimensionless numbers which characterize the flow conditions. The characteristic length and velocity are denoted by d and $\mathbf{u}_\infty$. As commonly used, ν stands for the kinematic viscosity of the fluid.

To model the turbulence a Large Eddy Simulation (LES) is chosen. Details regarding turbulence models can be found in Nezu et al. (1994). For the here described applications LES is viewed as the optimum for accuracy, computational efficiency and handling. A Smagorinsky (1963) approach is used as

3

a sub-scale model. Applying a space averaging filter (Sagaut, 2006) to the Navier-Stokes equations (1a) yields

$$\frac{\partial \overline{\mathbf{u}}}{\partial t} + \nabla \cdot (\overline{\mathbf{u}} \otimes \overline{\mathbf{u}}) = \frac{1}{Fr}\mathbf{g} - \nabla \overline{p} + \frac{1}{Re}\Delta \overline{\mathbf{u}} - \nabla \cdot \tau \qquad (4)$$

where $\overline{u}$ and $\overline{p}$ are the filtered quantities. Equation (4) now contains the additional sub-grid-scale tensor

$$\tau = -\nu_t \overline{D}_{ij} \qquad (5)$$

where the eddy–viscosity is denoted by $\nu_t = l^2 |\overline{D}|$ with $\overline{D} = \sqrt{\frac{1}{2}\overline{D}_{ij}\overline{D}_{ij}}$ and

$$\overline{D}_{ij} = \left(\frac{\partial \overline{u}_i}{\partial x_j} + \frac{\partial \overline{u}_j}{\partial x_i} \right) \qquad (6)$$

As the characteristic length l we use

$$l = C_s \sqrt{\Delta x^2 + \Delta y^2 + \Delta z^2}. \qquad (7)$$

The Smagorinsky constant C_s is set to $C_s = 0.0825$.

The Navier–Stokes equations are solved on a fluid domain Ω_f. The bottom of this domain is bounded by the sediment surface $h(x, y)$. This sediment surface h describes the height of the underlying sediment with respect to a reference plane (x, y) further below, compare Figure 1. To model the temporal change of the sediment surface h, we use the bed level equation postulated by Exner (1925), i.e.

$$\frac{\partial h}{\partial t} + \nabla \cdot \mathbf{q}_s(\tau(\mathbf{u})) = 0, \qquad (8)$$

where $\mathbf{q}_s(\tau(\mathbf{u}))$ is the transport rate function of the sediment. It depends on the shear stress τ, which is a function of the fluid velocity $\mathbf{u}$. Here, the shear

4
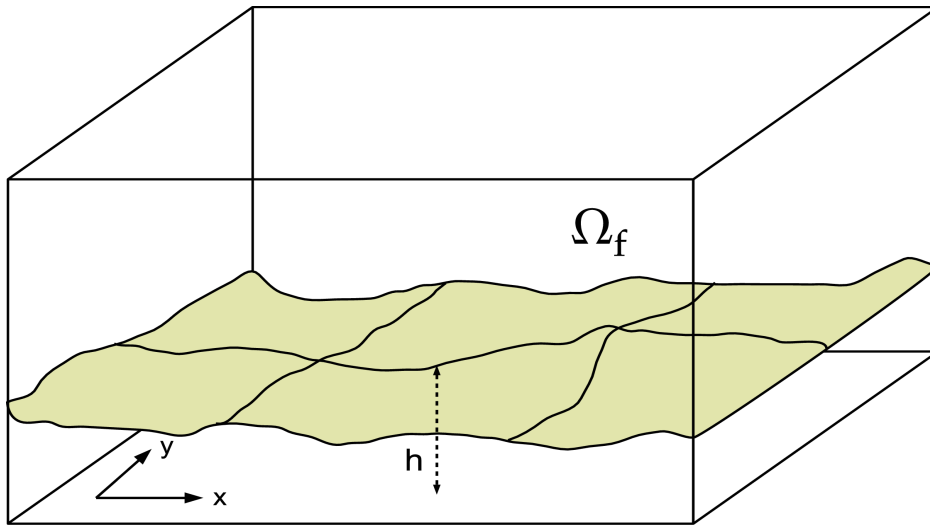
Figure 1: The sediment surface is described by the height $h(x, y)$, i.e. the distance from a underlying plane (x, y). Slopes are denoted by ∇h and can be computed directly. Thus, the fluid domain Ω_f is bounded by $h(x, y)$ from below.

stress function $\tau(\mathbf{u})$ is needed on the sediment surface. The Exner equation results from the conservation of mass and therefore from first principles. It states that the net balance between gain and loss of mass in a certain control volume results in a change of sediment height h. Several studies using the Exner equation to investigate the evolution of the geomorphology were conducted in, e.g. Parker (2004), Paola and Voller (2005), Kubatko et al. (2006), Kubatko and Westerink (2007). Moreover, Coleman and Nikora (2009) derived a version of Exner's equation from a statistical averaging process of a granular bed over time and in space.

The sediment surface determined by h denotes implicitly the fluid domain Ω_f. Thus, a change in h results in a change of the fluid domain Ω_f. Several models for the shear stress $\tau : \mathbb{R}^3 \mapsto \mathbb{R}^2$ and the bed load $\mathbf{q}_s : \mathbb{R}^2 \mapsto \mathbb{R}^2$ are

available in the literature, see Chanson (1999). In the following, we choose the empirically derived models (9a) and (9b)

$$\mathbf{q}_s = \sqrt{(s-1)gd_{50}^3} \cdot \left(\frac{4\tau(\mathbf{u})}{\rho_f(s-1)gd_{50}} - \tau_c \right)^{\frac{3}{2}}, \tag{9a}$$

$$\tau(\mathbf{u}) = \frac{1}{8}\rho_s\, f\, |\mathbf{u}|^2, \tag{9b}$$

where ρ_s denotes the sediment density, d_{50} is the median grain size, τ_c the dimensionless critical shear stress and $s = \rho_s/\rho_f$ with ρ_f as the fluid density. The velocity $\mathbf{u}$ is chosen at a distance y_τ from the sediment surface. The friction parameter is set according to Chanson (1999) as

$$f = \frac{64}{Re} \tag{10}$$

which is valid for flows with $Re < 2000$.

Equation (9a) is the modified version of the transport formula proposed by Meyer-Peter and Müller (1948), which has been validated by numerous experimental studies. The modification of the Meyer-Peter-Müller formula is proposed by Chanson (1999). Wong and Parker (2006) gave a nice review and reanalysis of (9a). Formula (9b) was presented in Chanson (1999).

Granular media like sand or silt have the property that unstable slopes are formed, if piled up. This instabiltity causes the surplus masses to slide down until a stable slope angle α_c establishes. This characteristic critical slope angle is influenced by different parameters, like shape, grain size, cohesion, moisture, and their interaction. This aspect needs to be reflected in a numerical model as well. Table 1 summarizes some slope angles for different sediment types collected from the literature (Julien, 1995).

Table 1: Selection of values for the critical angle of repose α_c (Möller et al. (2002), Julien (1995)). The large variety and the measuring of the values under water allows only rough estimates. This fact has to be taken into consideration when validating the numerical experiments.

sand	dry to wet	$20 - 45°$
gravel	roundness	$30 - 50°$
silt & clay	shape and roughness	$20 - 60°$

3. Numerical aspects: Discretization and Solver

For the numerical treatment of (4) and (1b), we employ the three dimensional parallel Navier-Stokes solver NaSt3D, see Griebel et al. (1998), with its recent improvements. NaSt3D is under development by Institute for Numerical Simulation at the University of Bonn. It features finite differences schemes on staggered grids like VONOS, ENO and WENO of up to fifth order for spatial derivatives in combination with second and third order time discretization schemes, like Adams-Bashforth and Runge-Kutta. The size of the time step is adaptively determined to fulfill a CFL condition, which is used for the whole spatial domain. Moreover, it uses the projection approach by Chorin (1967), which reduces the equations (4) and (1b) in each time step to a Poisson problem. The discretized Poisson equation reads as follows

$$\Delta_{dx}p = f \tag{11}$$

This Poisson problem is solved with a BiCG-Stab solver and after the correction of the projected velocities with ∇p a divergence-free velocity field is achieved, which enforces the incompressibility condition of the fluid. Domain decomposition with ghost cells is applied to parallelize the algorithm.

7

Two-phase fluid calculations are realized with a level set technique with local volume correction methods. After the transport of the level set function a reinitialization of the level set function is employed by solving the Hamilton-Jacobi equation, compare Croce (2002). The Hamilton-Jacobi equation reads as follows

$$\frac{\partial \phi}{\partial \tau} = sign(\phi_0) \left(1 - \|\nabla \phi\|_2\right) \tag{12}$$

where ϕ_0 the initial level set value. Here a third order Runge-Kutta and a fifth order WENO scheme are used. Solving this fix-point equation reconstructs a level set function, which obeys the distance property globally. Furthermore, a local volume correction is used to correct the volume of the level set phases after the reinitialization. For further information see Croce (2002), Croce et al. (2009), and Adelsberger et al. (2014). Griebel and Rüttgers (2013) and Griebel and Rüttgers (2014) studied the parallel performance of the code and achieved nearly optimal scale up and speed up for the NaSt3D code.

Furthermore, we discretize the bed level equation (8) similar to the setting used in NaSt3D. We employ second order finite difference schemes (SMART, QUICK) on a staggered spatial grid and second order explicit time discretization schemes (Adams–Bashforth). Whenever Ω_f changes in time, we have to update the fluid domain to couple the Navier–Stokes equations (4) and (1b) with the Exner equation (8). Here a loosely partitioned coupled approach is used, which couples the fluid solver on a given fluid domain with the bed level equation. The new sediment height h is treated by the first order obstacle representation of NaSt3D, which was previously described in Griebel et al. (1998).

Beside the discretization of the Navier–Stokes equations (4) and (1b) and

8

the Exner equation (8) we have to treat the slope failure behavior of the sand. Hill slope models are a topic of recent interest to simulate gravitational erosion of slopes. They have to take the characteristic critical slope angle α_c into account. Typical approaches were presented in, e.g. Lee and Herrmann (1993), Bouchaud et al. (1994), Alamino and Prado (2002), Seybold et al. (2007) and Perron (2011). In these studies the erosion is mainly driven by the shear stress caused by the flowing fluid. The collapse of slopes due to
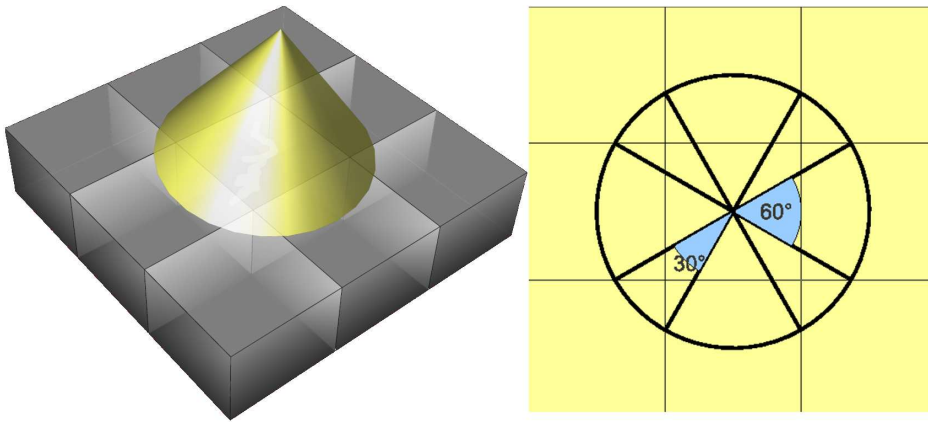
Figure 2: If the slope angle surpasses the critical angle $\alpha > \alpha_c$, surplus masses are distributed to the adjacent cells in each iteration step. Lateral cells are corrected with $\frac{1}{12}$ of the surplus masses and diagonal cells with $\frac{1}{24}$, which includes a safety factor of $\frac{1}{2}$. This process is iterated over the whole sediment surface until the limit condition (13) is fulfilled for each cell in each direction.

gravitation leads to a change in the calculated sediment height h. For this reason we restrict ourself to a slope limiting algorithm which preserves the angle, i.e. which ensures the condition

$$\arctan(\|\nabla h\|_2) \leq \alpha_c \tag{13}$$

and fits well to the setting of our fluid solver. Such a slope limiter is imple-

9

mented as an iterative algorithm. To this end, the slope angle is calculated locally after each physical time step of the simulation. If the critical value α_c is exceeded, the surplus masses are distributed to the adjacent cells. This process is iterated until all local angles observe the local limit condition (13). The schematic distribution process is illustrated in Figure 2. Note here that our slope limiter is mass conserving, limits the slopes to the critical angle of repose and leaves the other areas of the surface untouched, see also Figure 3. Side effects of the sliding sediment masses on the surrounding fluid are neglected.
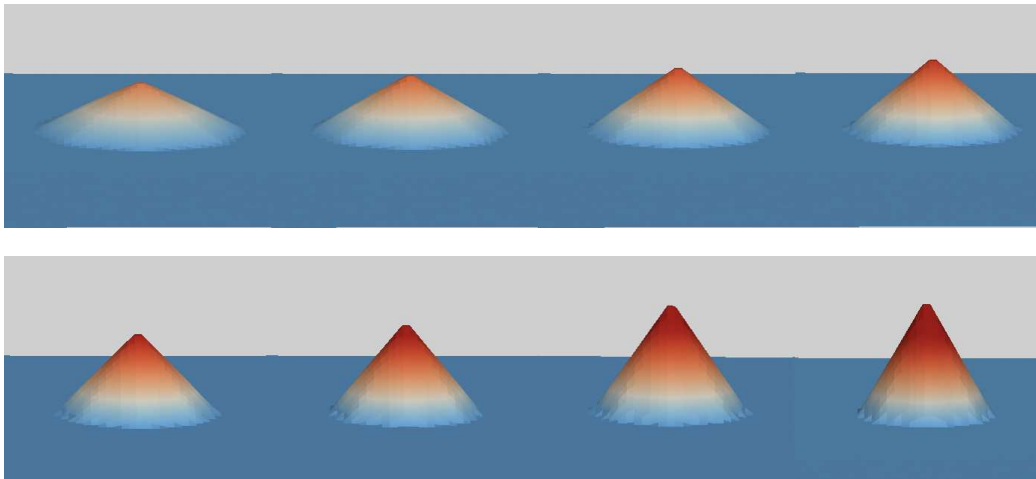
Figure 3: Results of 8 test simulations with slope limiting algorithm given a sediment pile and critical angles from $25°$ to $60°$. After $10 - 12$ iterations all angle conditions are fulfilled while the masses are conserved.

To achieve a robust and stable algorithm for the coupled problem ((1a), (1b), and (8)), we introduce an additional CFL condition according to Courant et al. (1928) for the bed level equation, i.e.

$$\Delta h < \min(\Delta x, \Delta y, \Delta z). \tag{14}$$

10

This condition is a restriction for the next time step and states that the change of sediment surface $\Delta h := h^{n+1} - h^n$ per time step Δt must not exceed the minimum size of a spatial cell. To ensure that the prediction does not fail, we multiply a security factor of 0.25 with Δt for the explicit discretization of the sediment model. In the numerical test, we observe that the time step size restriction from the Navier-Stokes solver is more restrictive. Compared with the sediment time step size a factor of 10^{-1} was observed. Nevertheless, if the transport parameters are chosen in extreme ranges the time step from the sediment solver restricts the Navier-Stokes solver. Thus, overall the minimum of both time steps is taken. Therefore the stability of the whole algorithm is assured. In this setting the loosely partitioned coupling algorithm reads as follows:

1. calculation of fluid properties (NaSt3D)
2. calculation of the shear stress τ and transport $\mathbf{q}_s$
3. solving Exner's equation (8)
4. limiting the local slope angles iteratively
5. mapping new h_{α_c} to geometry and adapting computational grid

A schematic view of the overall coupling is presented in Figure 4.

4. Numerical test and application to scouring at an obstacle

To test the presented algorithm and its implementation we compute a test case as illustrated in Figure 5. Here, the domain is a box closed on four sides. Two steps are situated at two opposing sides. Parabolic inflow and outflow profiles are applied above these steps. Additionally a rectangular obstacle
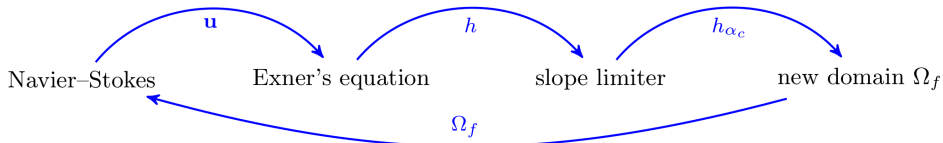
Figure 4: Flow chart of our loosely partitioned coupling algorithm in each time step, the velocities from NaSt3D are used to calculate the new sediment height h, which, after correcting to h_{α_c} due to the slope limiter iteration, determines the new Ω_f and therefore the new fluid domain.

is placed at the right side of the box. The bottom of the box is filled with sediment of half the height of the steps. We simulate the erosion in this water tank for four different grid sizes ($48 \times 32 \times 32$, $72 \times 48 \times 48$, $108 \times 72 \times 72$ and $162 \times 108 \times 108$). The results are shown in Figure 6. Due to our choice of grids, we have the factor of $\frac{3}{2}$ for refinement from one grid to the next. Moreover, with this special choice of the grids it is assured that the boundary of the physical domain is exactly resolved by all four discretizations. Thus the discretized domain is truly the same on all grids.

The HPC cluster used to compute the result is the *Siebengebirge* which has 5 Dell PowerEdge R910 computing nodes with 160 Intel Xeon X7560 2.226 GHz CPU cores and a main memory of 2560 GB in total, i.e. one computing node contains 32 CPU cores and has 512 GB main memory. Mellanox ConnectX Infiniband realises the MPI communication on Siebengebirge. A Linpack performance test of the system resulted in 1349 GFlops/s with a parallel efficiency of 93%. In the following we used 32 cores for 24 h to compute the finest grid solution. In all time steps the residual for the solution of the pressure equation converged to

$$\|f - \Delta_{dx} p_{it}\|_2 = 10^{-10} \tag{15}$$

12

To measure the numerical error we interpolate the numerical solutions of h on the first three grids ($48 \times 32 \times 32, 72 \times 48 \times 48$ and $108 \times 72 \times 72$) to the finest grid ($162 \times 108 \times 108$) and calculate the pointwise norm

$$\|h\|_2 = \sqrt{\sum_{i=1}^{162} \sum_{j=1}^{108} \left(h_{i,j}^{int} - h_{i,j}^{fine} \right)^2} \tag{16}$$

there. The interpolations of the coarser solutions to the finest grid were computed with a cubic interpolation scheme. We observe that the decay of the error is of the order $(\Delta x)^{0.818}$, which comes close to a first order rate. The resulting errors are presented in Figure 7. Here the first order obstacle representation of NaSt3D, which interferes with the fluid solver during the coupling algorithm, seems to prevent higher rates. A higher order approximation technique for the geometry of the obstacles could help to improve this rate. Another value deduced from this test scenario is the conservation of the sediment masses. The temporal evolution of total sediment mass is plotted in Figure 8. After $50\,s$ the differences to the initial mass do not exceed 0.02%. Thus, the numerical schemes can clearly be considered as mass conserving.
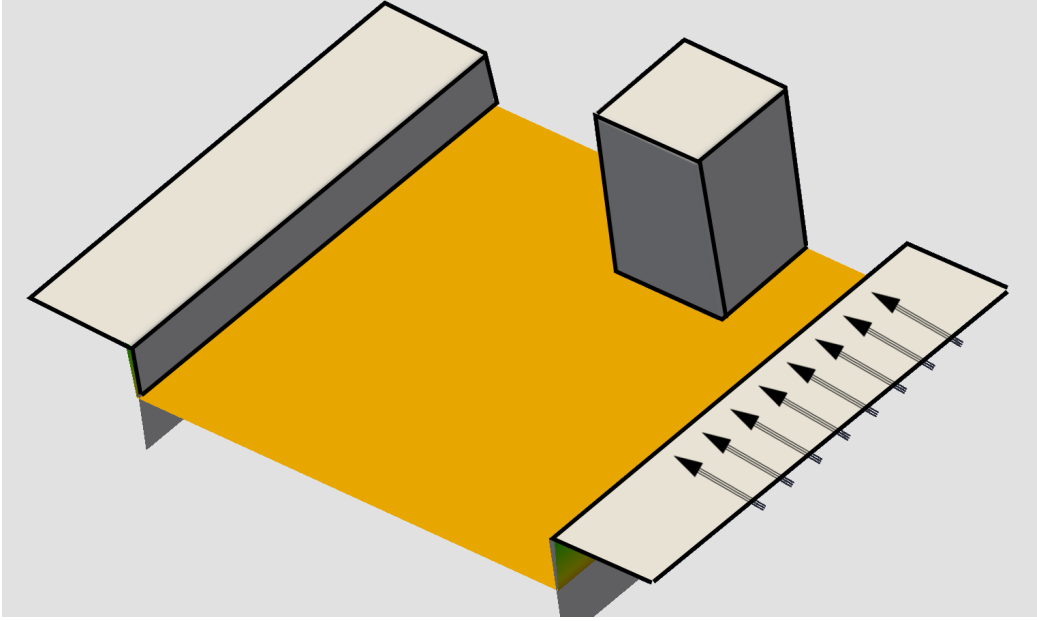
Figure 5: Start configuration of the test case. A rectangular obstacle is placed in a sediment filled box, which is closed at the sides. Parabolic inflow and outflow profiles are applied above the steps. No-slip boundary conditions to model the friction are imposed to the sediment surface and the obstacle. Furthermore, the steps prevent the sediment from leaving the domain. The physical size of the domain is chosen as $243m \times 162m \times 162m$ with an obstacle size of $40m$ and an inflow velocity of $3m/s$. Reynolds number is set to $Re = 100$. For the sedimentary properties we choose $d_{50} = 0.1m$, $\tau_c = 0.0047$, and $y_\tau = 3.1m$. With this setting the physical domain is exactly resolved on all discretization grids.
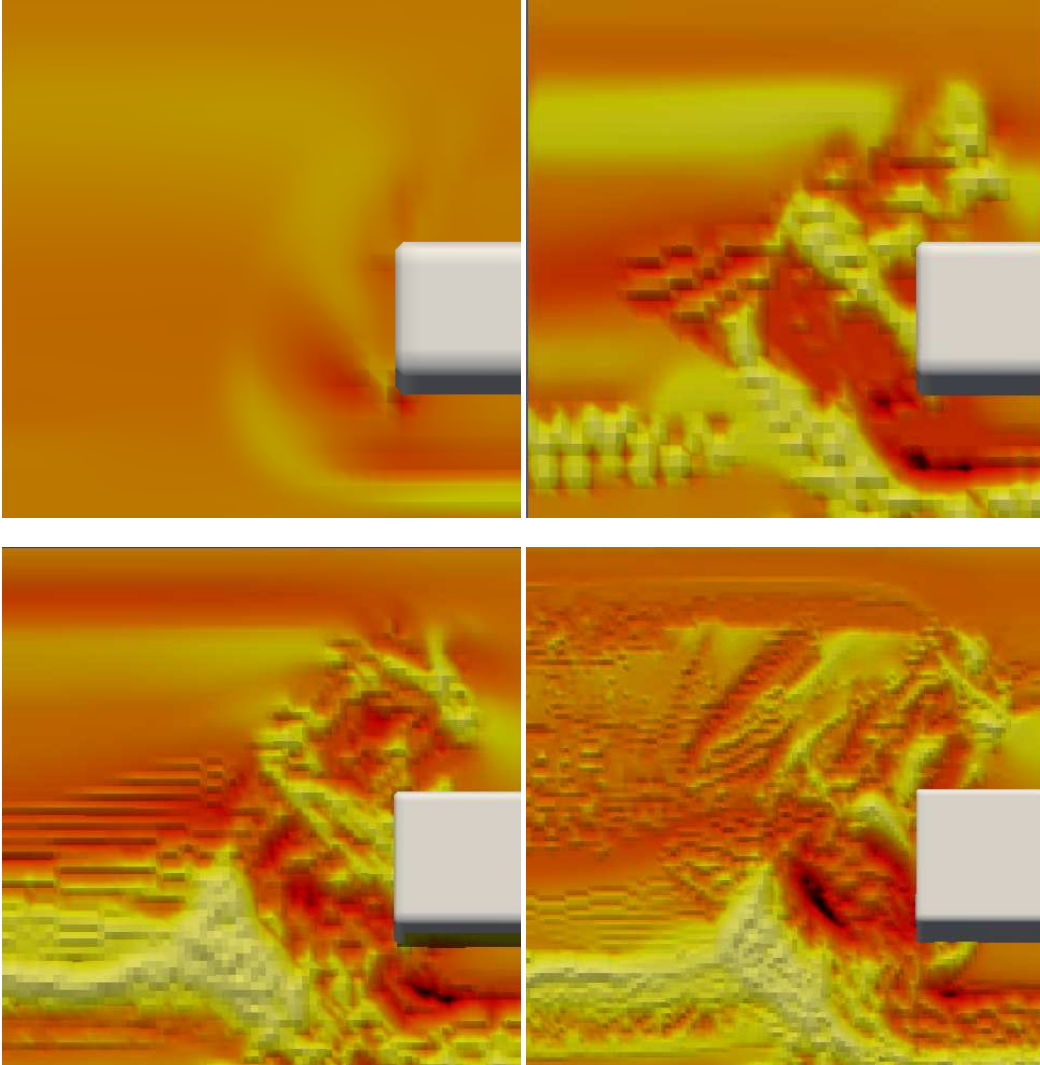
Figure 6: Visualization of the sediment height from top view after $50\,s$ on the different grids. From the left to the right and from top to bottom the resolutions are ($48 \times 32 \times 32$, $72 \times 48 \times 48$, $108 \times 72 \times 72$ and $162 \times 108 \times 108$). The main sedimentary features of a scour mark at the obstacle are recovered in all resolutions. Additionally the finest example shows fine sedimentary structures beside the obstacle.
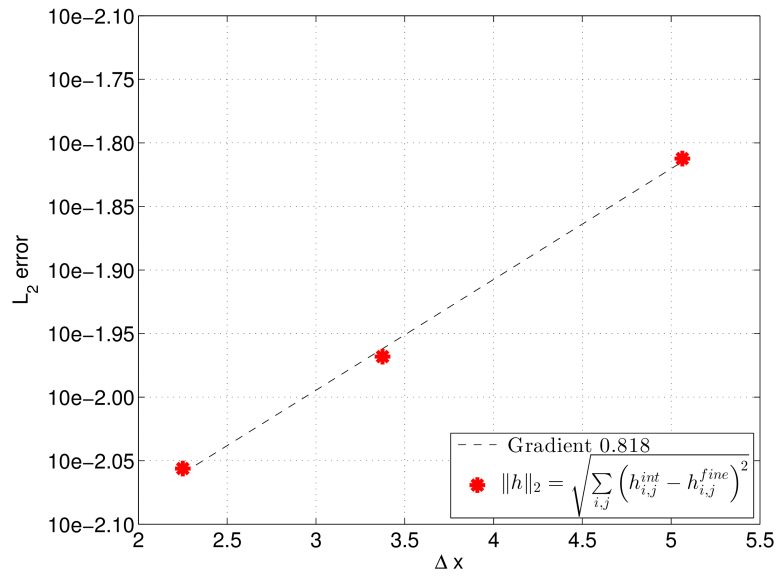
Figure 7: $\|\cdot\|_2$-error of the sediment surface h after $50\,s$ for 3 different grids on the finest grid on our test case scenario of Figure 5. The error is of the order 0.818. The gradient of the line was calculated by $\|\cdot\|_2$ best approximation.
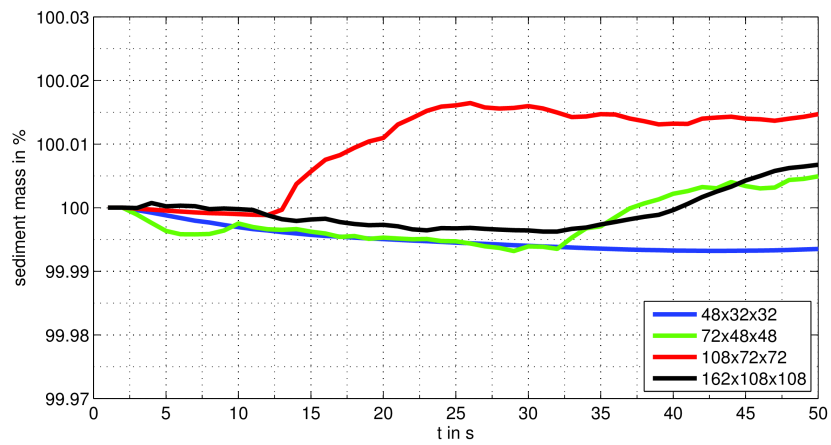
Figure 8: Temporal evolution of the total sediment mass on the four grids. The sediment mass is conserved up to 0.02%. The differences of the masses are in the range of the numerical discretization error and can be regarded as numerical artefacts.

17

We now apply our new numerical method to a real life problem from hydraulic engineering, namely the scouring at an obstacle. Fluvial obstacle marks are defined as the combination of a scour, i.e., the erosional part at an obstacle, with its corresponding sediment ridge, i.e., the depositional part. Figure 9 shows an example of a fluvial obstacle mark at a rectangular obstacle studied in the laboratory flume at the Department of Geography, University of Bonn. For the numerical simulation of a fluvial obstacle mark, there are several articles in the literature, where scouring in front of or beneath an obstacle is computed (Link (2006), Amoudry and Liu (2009), Adhikary et al. (2009), Huang et al. (2009), Liu and Garcia (2006)). Other numerical studies investigated the scouring beside obstacles (Zhang et al., 2005), the erosion in river bends (Wu and Wang, 2005) or the geomorphological evolution in general (Long et al. (2008), Duc and Rodi (2008)). In most of these studies the purpose was to predict the erosional process but the deposition of the entrained material was neglected. Recent numerical works by Khosronejad et al. (2012) and Dixen et al. (2013) studied scouring at obstacles where both processes were considered. Our goal is to also treat both processes and to thus give a more detailled insight into the interaction of the flow and the sediment body. To this end, note that our model is indeed capable of reproducing erosion as well as deposition.

We test our algorithm for an example, which is a scaled-up version of an experiment with a rectangular obstacle (Figure 9). We consider a channel-like computational domain of 5.0 meters width and 5.0 meters height. As computational grid we choose $800 \times 100 \times 100$. Furthermore, we choose fine sand grains ($d_{50} = 0.0001\,m$) and a critical shear stress $\tau_c = 0.0001\,N/m^2$.

The thickness of the initial sediment bed is 1.25 meters. As obstacle we model a block of 1.0 meter in length and width, its height is 1.25 meters, compare Figure 10. We compute a physical time of $450\,s$ in our simulation. The computational time is limited to $180\,h$ on 64 CPU cores of *Siebengebirge*. The boundary conditions at the sediment surface, the top, and at both side walls are set to slip boundary conditions. This results in frictionless boundaries for this experiment. In contrast, no-slip boundary conditions are applied to the rectangular obstacle. For the inflow wall we apply a standard parabolic profile. To achieve an open wall at the end we set Neumann zero boundary condition to the outlet.

Altogether, we have a fully submerged stationary obstacle with analogous distance to the fluid surface as in the flume experiment of Figure 9. All fluid properties are scaled properly to achieve comparability (Table 11). Laboratory flumes have to be large-dimensioned so that a sufficiently developed flow situation establishes before the flow reaches the obstacle. To meet this requirement we use 40 meters as the length of our flow domain in the numerical simulation. The inflow velocity is set to $1\,m/s$. The Reynolds number is set to $Re = 1000$.

Furthermore, we choose the WENO fifth order scheme (Shu, 1999) to discretize the spatial parts of the flow model and we use a second order Adams–Bashforth time scheme. For the discretization of the Exner equation we use the SMART second order scheme (spatial) and the second order Adams–Bashforth scheme in time. A summary of the employed parameters and the experimental setup is given in Figure 10. A typical snapshot of the resulting vortex system around the obstacle is presented in Figure 13. The downward

vortex in front of the obstacle causes an increase of the shear stress and the sediment is eroded there. As observed by Euler (2007) the sediment is entrained by the fluid and is transported with the inherent horseshoe vortex system. With decreasing velocities in the lee, particles settle down and form a symmetric ridge. Comparing Figures 12 with Figure 9, we observe an excellent agreement of our simulation results with that in the laboratory flume. In the temporal evolution of the numerical simulation we observe an initial increase of the shear stress in front of the obstacle. This temporal increased shear stress causes a deepening of the scour which in turn causes a decrease in the shear stress afterwards. The basic form of the scour mark as well as the depositional ridge has formed in the first $75\,s$. After this initial phase we observe a decrease in the intensity of τ which is distributed more regularly over the whole domain. The decline of the shear stress and the new distribution leads to a stretching of the whole bedform. The scour depth and the height of the sediment ridge support this observation. After an intense phase of erosion and deposition, the depth of the scour and height of the sediment ridge tend to stabilize over the simulation time (Figure 15). The asymmetries of the shear stress distribution result from the turbulent flow. Despite the small asymmetries at the tips of the sediment ridge the scour mark can be regarded as symmetrically. These observations are in good agreement with experimental results presented by Euler (2007) and Euler and Herget (2011). In Figure 14 a comparison of the measured data and the numerical simulation are given.
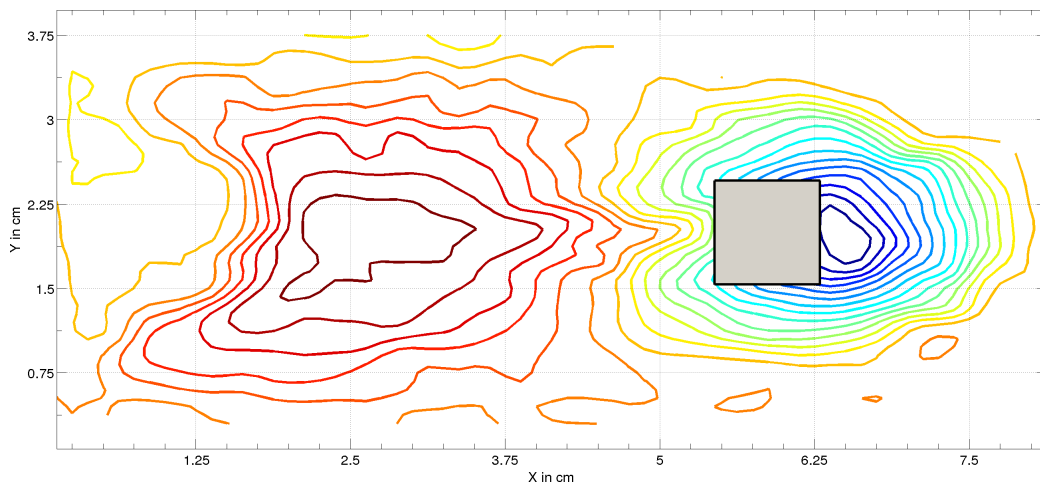
Sediment height contours of scour mark from flume experiment.
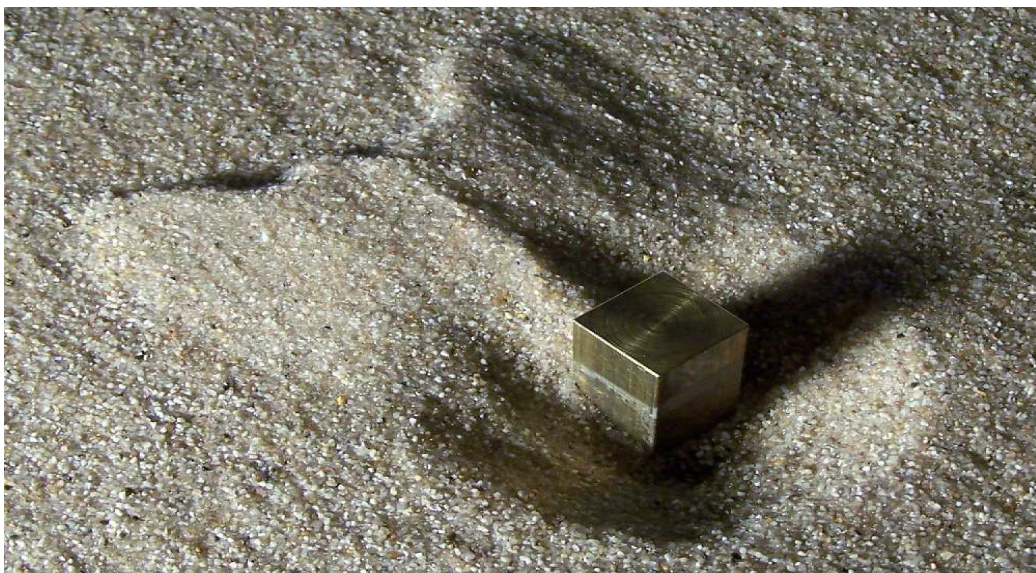
Figure 9: Scour mark at a rectangular obstacle. Laboratory work in a flume, Dep. of Geography, University of Bonn. The Flow direction is from the bottom right to the top left corner. An erosional depression in front of and a depositional ridge behind the obstacle show up. The size of the rectangular obstacle is $(l \times w \times h)$ $1\,cm \times 1\,cm \times 1.25\,cm$. The grain size of the sediment is $0.001\,cm$. For further details of the flume properties see Euler and Herget (2011).

$l{\times}w{\times}h$	dimensions (in m)	$40 \times 5 \times 5$	$\mathbf{q}_s$	transport equation	MPM
u_{in}	inflow velocity	$1\,m/s$	Re	Reynolds number	1000
ρ_f	fluid density	$1000\,kg/m^3$	dx	spatial resolution	$0.05\,m$
ρ_s	sediment density	$2650\,kg/m^3$	flow	(spatial) scheme	WENO ($5th$)
d_{50}	mean grain size	$0,0001\,m$	sedimen	(spatial) scheme	SMART ($2nd$)
τ_c	critical shear stress	$0,0001\,N/m^2$	flow + sed	(temporal) scheme	AB ($2nd$)
	Resolution	$800/100/100$		Poisson–Solver	BiCG–Stab

Figure 10: Parameters and experimental start configuration. A block ($1.0\,m \times 1.0\,m \times 1.25\,m$) is placed in the middle of the domain. Flow velocity is set to $1\,m/s$. The grid resolution is $800 \times 100 \times 100$. The distance y_τ to the sediment surface where the local bed velocities are evaluated is set to $0.1\,m$. A critical angle of repose of $\alpha = 40°$ is chosen a as generic value.

	flume data	numerical experiment	
l	$0.01\,m$	$1\,m$	characteristic length
u	$0.135\,m/s$	$1\,m/s$	mean flow velocity
ν	$1.3 \cdot 10^{-6} m^2/s$	$10^{-3}\,m^2/s$	kinematic viscosity ($11°C$)
Re	1038	1000	Reynolds number

Figure 11: Flow and geometry parameters for the numerical experiment in comparison with the flume data set. The flume experiments were conducted in the laboratory flume at the Department for Geography, University Bonn. Other results from similar experiments in this flume were presented in Euler (2007) and Euler and Herget (2011).

10 s   50 s

75 s   150 s

300 s   450 s
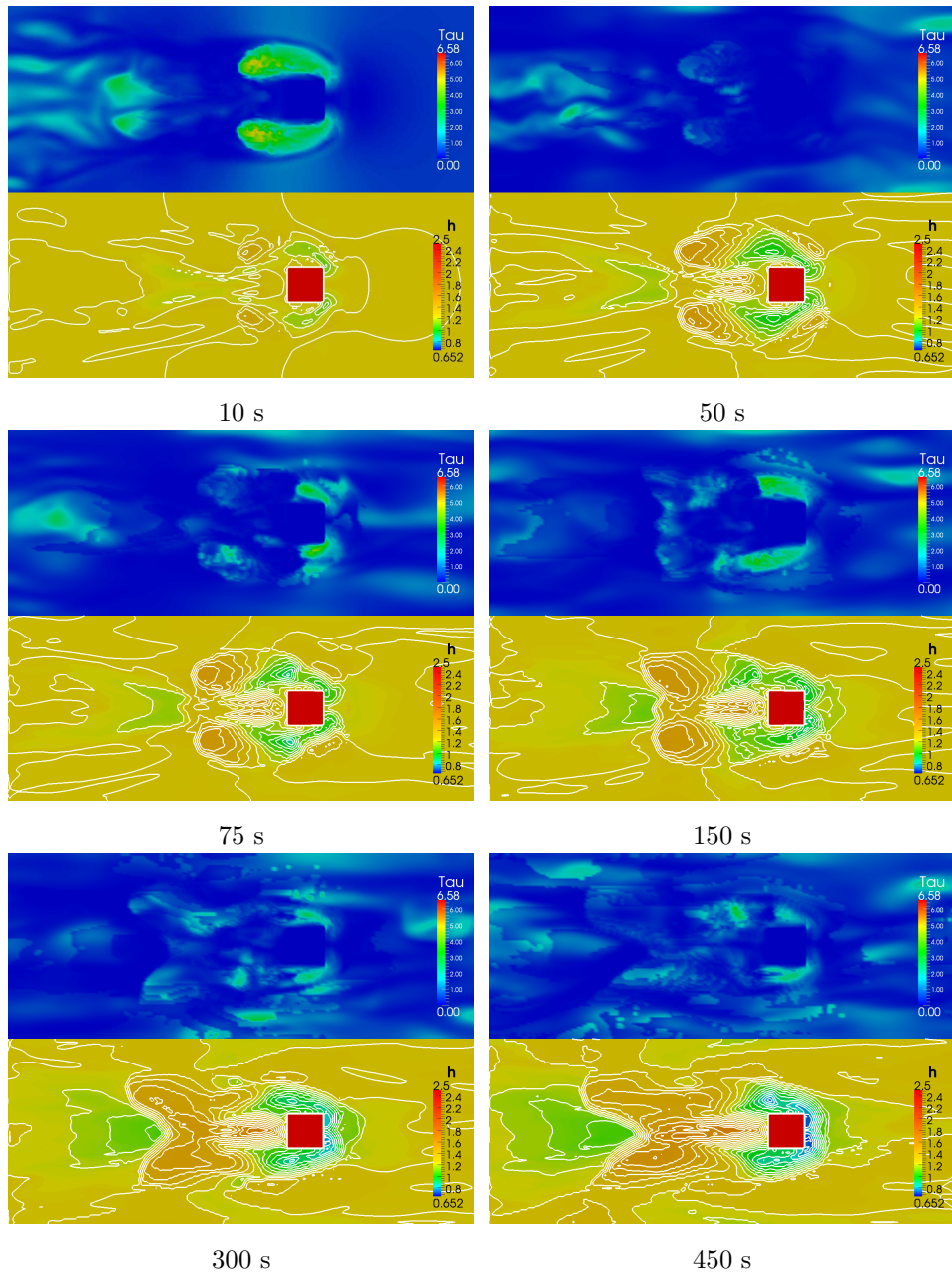
Figure 12: Shear stress τ and sediment height h over time. The flow direction in each Figure is from right to left. Only the relevant part around the scour mark is visualized. The inflow region which is needed to have fully developed uniform flow situation is not shown. Starting with a plain sediment bed, the basic structure of the scour mark develops in the first $75\,s$. The maximum shear stress is concentrated at the top of the evolving sediment ridge.

23
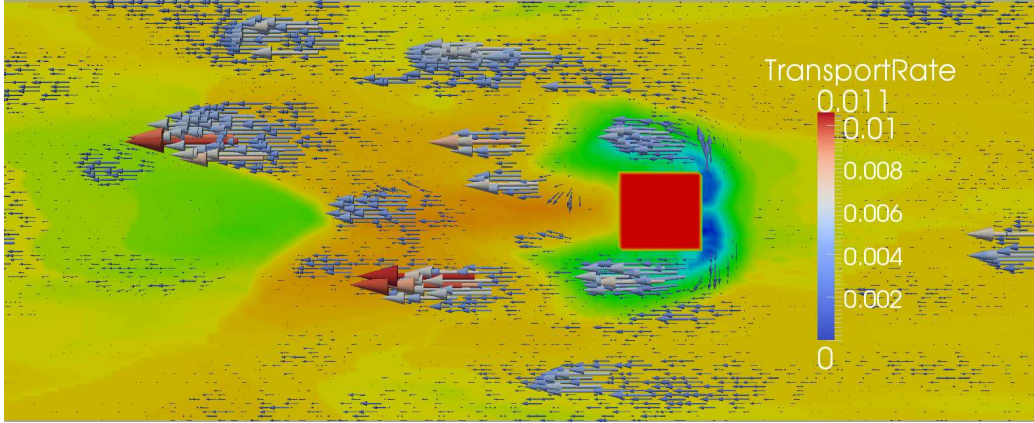
(a) Transport rates $\mathbf{q}_s$ at the sediment bed
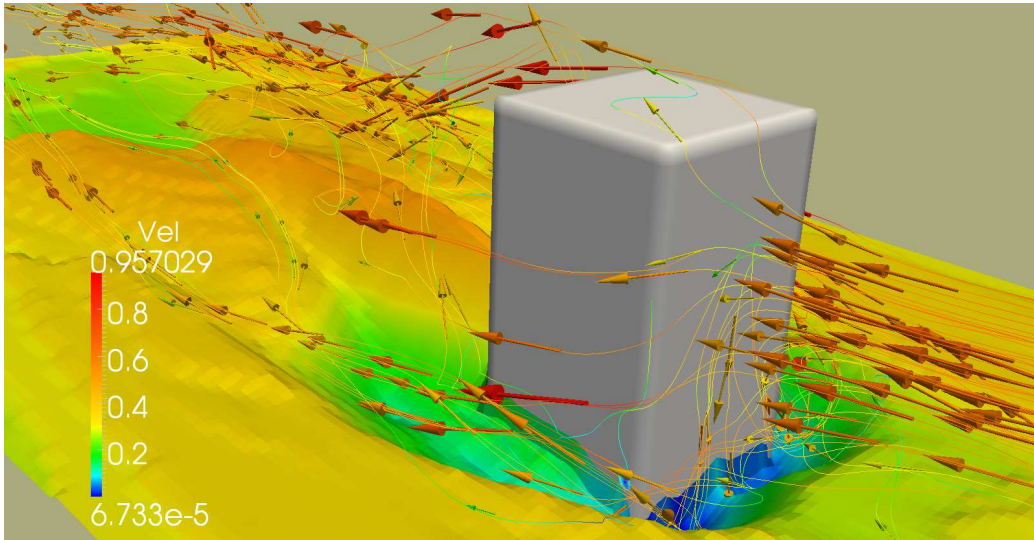
(b) Simulated vortex system of the flow near the obstacle at $450\,s$.

Figure 13: The typical separation of the flow in front of the obstacle to the sides as well as into downward and upward flow is well reproduced in comparison with laboratory experiments with similar geometries from the literature, see Euler and Herget (2011). The transport rates reflect the turbulent flow. Sediment is not in transport at locations in the observation site where τ_c is not reach. Note that the transport in the scour hole is mainly at the edges and at the sides.
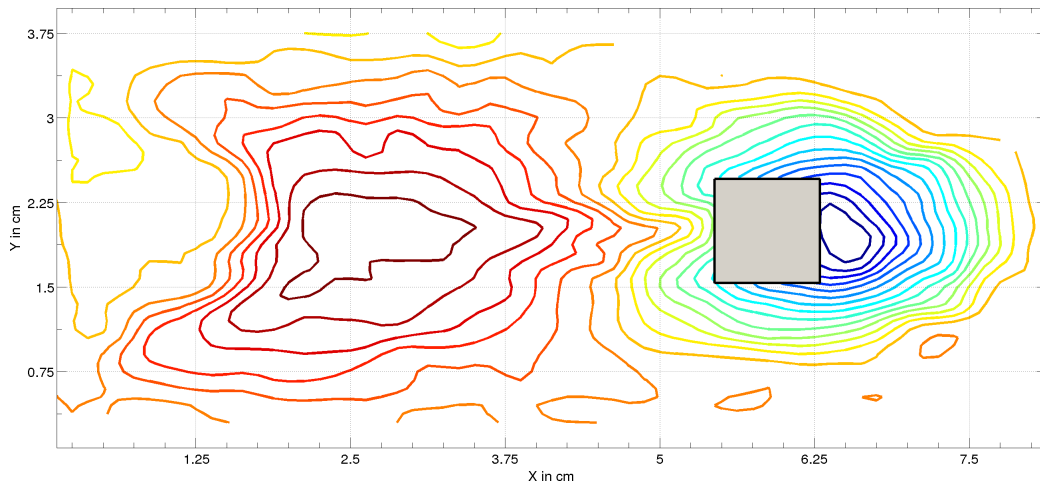
Contours of the sediment surface in the flume experiment
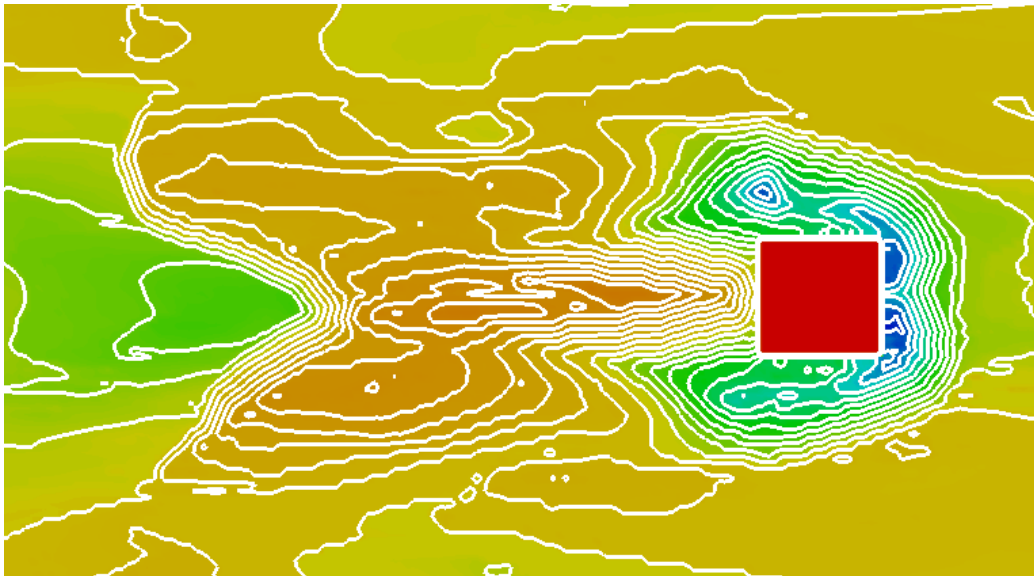
Isocontours of the sediment height visualized from the dimensionless numerical experiment

Figure 14: The comparison of flume measurements (top) with the numerical study (bottom) show proper agreement of the computed sediment heights with the experimental measurements. The numerical experiment reproduces the basic features of a deposition as well as a erosion site. Furthermore small scale features are also well captured, e.g. the crescent shaped end of the sediment ridge or the erosional parts beside the obstacle. The scour length is slightly underestimated by the numerical experiment.
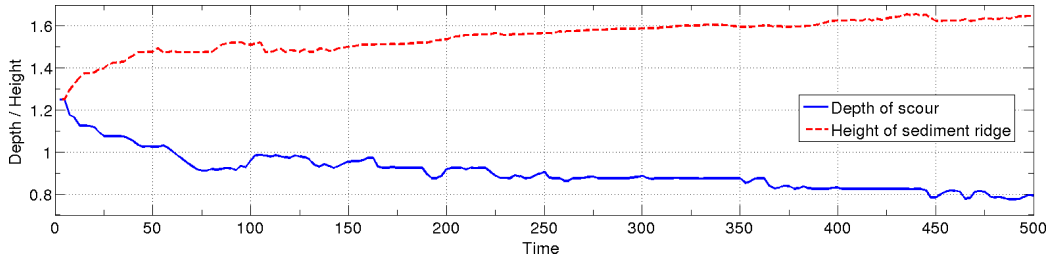
Figure 15: Evolution of the scour depth (blue solid) and the height of the leewise sediment ridge (red dashed). After a short intense period of redistribution of the sediment until $75\,s$, the depth of the scour as well as the ridge height increase slowly. A stagnation and therefore a fully stable sediment form was not observed until the end of simulation. Similar results were found in experimental studies conducted in a laboratory flume by Euler and Herget (2011).

5. Conclusion

We presented a three dimensional model for current-driven sediment processes and their resulting bedforms. Exner's bed level equation and the Navier–Stokes equations were discretized with a finite difference approach on a staggered grid. To take turbulent effects into account a LES turbulence model with Smagorinsky approach was implemented. A slope limiting iterative process was introduced to secure the slope angles of the sediment. We applied a fifth order scheme in space and a second order discretization scheme in time. The equations were treated explicitly in each time step, which resulted in a CFL condition and altogether gave a loosely coupled overall algorithm. In a test case scenario we were able to show that the sediment mass is conserved. The error analysis with successive finer grid solutions showed that error converged with a rate of 0.818. With this algo-

26

rithm, we computed a three-dimensional real life example of the scouring at an obstacle. The numerical simulation reproduced the typical evolution of a scour mark. The depth of the scour, the height of the ridge and the basic bed form were neatly recovered. We observed the typical vortex system responsible for the sediment transport and its interaction with shear stress and transport rates. These results were in good agreement with laboratory work. Altogether, our new numerical approach promises to simulate other real life bedforms and sedimentary processes with sufficient accuracy.

6. References

Adelsberger, J., Esser, P., Griebel, M., Groß, S., Klitz, M., Rüttgers, A., 2014. 3D incompressible two-phase flow benchmark computations for rising droplets. In: Onate, E., Oliver, X., Huerta, A., (Eds.), Proceedings of the 11th World Congress on Computational Mechanics (WCCM XI), Barcelona, Spain. 5274–5285.

Adhikary, B. D., Majumdar, P., Kostic, M., 2009. CFD simulation of open channel flooding flows and scouring around bridge structures. In: Xi, L. (Ed.), Proceedings of the 6th WSEAS International Conference on FLUID MECHANICS (FLUIDS'09). pp. 114–120.

Alamino, R. C., Prado, C. P., 2002. Some considerations on the Bouchaud–Cates–Ravi–Edwards model for granular flow. Physica A: Statistical Mechanics and its Applications 308 (1-4), 148–160.

Amoudry, L., Liu, P.-F., 2009. Two-dimensional, two-phase granular sed-

iment transport model with applications to scouring downstream of an apron. Coastal Engineering 56, 693–702.

Bouchaud, J.-P., Cates, M. E., Ravi, J. R., Edwards, S. F., 1994. A model for the dynamics of sandpile surfaces. Journal de Physique I 4, 1383–1410.

Chanson, H., 1999. The Hydraulics of Open Channel Flow - An Introduction. Edward Arnold, London.

Chorin, A. J., 1967. A numerical method for solving incompressible viscous flow problems. Journal of Computational Physics 2 (1), 12–26.

Coleman, S. E., Nikora, V. I., 2009. Exner equation: A continuum approximation of a discrete granular system. Water Resource Research 45, 1–8.

Courant, R., Friedrichs, K., Lewy, H., 1928. Über die partiellen Differenzengleichungen der mathematischen Physik. Mathematische Annalen 100 (1), 32–74.

Croce, R., 2002. Ein paralleler, dreidimensionaler Navier-Stokes-Löser für inkompressible Zweiphasenströmungen mit Oberflächenspannung, Hindernissen und dynamischen Kontaktflächen. Diplomarbeit, Insitut für Numerische Mathematik, Universität Bonn.

Croce, R., Griebel, M., Schweitzer, M. A., 2009. Numerical simulation of bubble and droplet-deformation by a level set approach with surface tension in three dimensions. International Journal for Numerical Methods in Fluids 62 (9), 963–993.

Dixen, M., Sumer, B. M., Fredsoe, J., 2013. Numerical and experimental investigation of flow and scour around a half-buried sphere. Coastal Engineering 73, 84–105.

Duc, B., Rodi, W., 2008. Numerical simulation of contraction scour in an open laboratory channel. Journal of Hydraulic Engineering 134 (4), 367–377.

Euler, T., 2007. Kolke an überströmten Hindernissen als fluviale Gerinnebettformen - Experimente im hydraulischen Versuchskanal. Master's thesis, Geographisches Institut Universität Bonn.

Euler, T., Herget, J., 2011. Obstacle-Reynolds-number based analysis of local scour at submerged cylinders. Journal of Hydraulic Research 49 (2), 267–271.

Exner, F. M., 1925. Über die Wechselwirkung zwischen Wasser und Geschiebe in Flüssen. Sitzungsbericht Akademie der Wisssenschaft Wien 134, 165–180.

Griebel, M., Dornseifer, T., Neunhoeffer, T., 1998. Numerical Simulation in Fluid Dynamics, a Practical Introduction. SIAM, Philadelphia.

Griebel, M., Rüttgers, A., 2014. Simulation of dilute polymeric fluids in a three-dimensional contraction using a multiscale FENE model. Proceedings of PPS-29: The 29th International Conference of the Polymer Processing Society, Nuremberg, Germany, 539–543.

Griebel, M., Rüttgers, A., 2013. Multiscale simulations of three-dimensional

viscoelastic flows in a square-square contraction. Journal of non-Newtonian Fluid Mechanics. Vol. 205. 41-63.

Huang, W., Yang, Q., Hong, X., 2009. CFD modeling of scale effects on turbulence flow and scour around bridge piers. Computers & Fluids 38, 1050–1058.

Julien, P., 1995. Erosion and Sedimentation. Cambridge University Press, Cambridge.

Khosronejad, A., Kang, S., Sotiropoulos, F., 2012. Experimental and computational investigation of local scour around bridge piers. Advances in Water Resources 37 (0), 73 – 85.

Kubatko, E. J., Westerink, J. J., 2007. Exact discontinuous solutions of Exner's bed evolution model: Simple theory for sediment bores. Journal of hydraulic engineering 133 (3), 305–311.

Kubatko, E. T., Westerink, J. J., Dawson, C., 2006. An unstructured grid morphodynamic model with a discontinuous Galerkin method for bed evolution. Ocean Modelling 15, 71–89.

Lee, J., Herrmann, H., 1993. Angle of repose and angle of marginal stability: molecular dynamics of granular particles. Journal of Physics A: Mathematical and General 26 (2), 373–383.

Link, O., 2006. Untersuchung der Kolkung an einem schlanken zylindrischen Pfeiler in sandigem Boden. Ph.D. thesis, Fachbereich Bauingenieurwesen und Geodäsie der Technischen Universität Darmstadt.

Liu, X., Garcia, M., 2006. Numerical Simulation of Local Scour with Free Surface and Automatic Mesh Deformation. American Society of Civil Engineers, Ch. 58, pp. 1–10.

Long, W., Kirby, J. T., Shao, Z., 2008. A numerical scheme for morphological bed level calculations. Coastal Engineering 55, 167–180.

Meyer-Peter, E., Müller, R., 1948. Formulas for bed-load transport. In: Proceedings of the 2nd Meeting of the International Association for Hydraulic Structures Research. IAHR, Stockholm, Sweden, pp. 39–64.

Möller, L. E., Kuhlman, K. R., Marshall, J. R., Towner, M. C., 2002. The snoopy angle of repose experiment: Calibration of an instrument to determine the angle of repose of Martian dust. Lunar and Planetary Science 33.

Nezu, I., Nakagawa, H., and Jirka, G. 1994. Turbulence in open-channel flows. Journal of Hydraulic Engineering, 120(10), 1235–1237.

Paola, C., Voller, V., 2005. A generalized Exner equation for sediment mass balance. Journal of geophysical Research: Earth Surface 110 (F4).

Parker, G., 2004. 1D Sediment Transport Morphodynamics with Applications to Rivers and Turbidity Currents. e-book.

Perron, J. T., 2011. Numerical methods for nonlinear hillslope transport laws. Journal of Geophysical Research: Earth Surface 116 (F2).

Sagaut, P. (2006). Large Eddy Simulation for Incompressible Flows: An Introduction. Scientific Computation. Springer.

Seybold, H., Andrade, J., Hermann, H., 2007. Modeling river delta formation. In: Proceedings of the National Academy of Sciences of the United States of America. Vol. 104. pp. 16804–16809.

Shu, C.-W., 1999. High order ENO and WENO schemes for computational fluid dynamics. In: Barth, T., Deconinck, H. (Eds.), High-Order Methods for Computational Physics. Vol. 9 of Lecture Notes in Computational Science and Engineering. Springer Berlin Heidelberg, pp. 439–582.

Smagorinsky, J. 1963. General circulation experiments with the primitive equations. Mon. Wea. Rev., 91, 99–164.

Wong, M., Parker, G., 2006. Reanalysis and correction of bed-load relation of Meyer-Peter and Müller using their own database. Journal of Hydraulic Engineering 132, 1159–1168.

Wu, W., Wang, S. S., 2005. Development and applications of NCCHE's sediment transport models. In: US-China Workshop on Advanced Computational Modelling in Hydroscience & Engineering.

Zanke, U., 2002. Hydromechanik der Gerinne und Küstengewässer - Für Bauingenieure, Umwelt- und Geowissenschaftler. Parey Buchverlag, Berlin.

Zhang, H., Nakagawa, H., Ishigaki, T., Muto, Y., Baba, Y., 2005. Three-dimensional mathematical modeling of local scour. Journal of Applied Mathematics 8, 803–812.